Preparation of supported catalysts: a study of the effect of small amounts of silica on Ni/Al_2O_3 catalysts

Gabriella Garbarino[1], Sahar Chitsazan[1], Thanh Khoa Phung[1,2], Paola Riani[3], and Guido Busca[1]*

1 Università degli Studi di Genova, Dipartimento di Ingegneria Civile, Chimica e Ambientale (DICCA), P.zzale Kennedy, 1 16129 Genova, Italy
2 NTT Institute of Hi-Technology (NIH), Nguyen Tat Thanh University, 298-300A Nguyen Tat Thanh Street, Ward 13, District 4, Ho Chi Minh City, Vietnam
3 Università degli Studi di Genova, Dipartimento di Chimica e Chimica Industriale (DCCI), Via Dodecaneso, 31 16146 Genova, Italy

*phone +390103536024; fax +390103536028; e-mail: Guido.Busca@unige.it

Keywords: Nickel catalysts; alumina support; silica-doped alumina; reducibility of Ni catalysts; ethanol steam reforming; supported catalysts.

Abstract. Nickel catalysts supported on pure alumina (Puralox) and 5% silica-containing alumina (Siralox) have been prepared, characterized (XRD, UV-vis-NIR, IR, H_2-TPR and FE-SEM) and tested. It is confirmed that small amounts of silica hinder the surface area loss of alumina upon calcination, allowing the retention of higher surface areas also when NiO is deposed on the support. Depending on the Ni loading, calcination temperature and on the presence/absence of silica, several species of Ni^{2+} are formed on the catalyst: highly dispersed ions, Ni-aluminate defective spinel species and NiO particles. The presence of 5% silica hinders the dispersion of Ni^{2+} ions and the formation of Ni aluminate phase, and favours the formation of the NiO phase. This is attributed to the competition of silica and nickel oxide for interaction on the most reactive surface sites of alumina. Silica shifts Ni species to less reactive sites where the Ni-alumina interaction is weaker. As a result of this, the addition of silica to alumina supports gives rise to more easily reducible Ni catalysts, that become active in Ethanol Steam Reforming at lower temperature.

1. Introduction

Oxide-supported oxides represent relevant materials in the catalysis field, both as catalysts (e.g. like for oxidation catalysis [1]) and as catalyst precursors. In fact most of

supported metal [2] and sulphide catalysts [3] are first produced in the form of supported metal oxides and then undergo activation procedures by reduction and /or sulphidation treatments.

As reported for a number of oxide-supported on oxide systems, when the support is well dispersing (such as e.g. for alumina, zirconia, titania carriers) and loading is low with respect to the carrier surface area, impregnation procedures produce atomically dispersed species (sometimes denoted as “monolayers”). Above a certain loading limit, bulk supported oxide nanoparticles start to be formed.

However, in most industrial catalysts preparations, a number of components, are deposed on the surface of the support besides the active phase(s), such as stabilizers, activators, etc. As discussed years ago for the V_2O_5-WO_3-K_2O/TiO_2 system [4], in some way supported species compete for anchoring on the more reactive surface sites at the surface of support. According to recent studies [5,6], it seems likely that on the alumina surface the most active surface sites are on edges, corners and defects of the oxide structure, the sites located on plain faces being likely less reactive. Over the defect sites the deposed species would first interact, while at higher coverages they also occupy less reactive sites.

Silica is a common additive of aluminas mainly to stabilize Al_2O_3 against loss of surface area [6]. The presence of small amounts of silica on the alumina support may modify the dispersion of the active phases with a resulting modification of the final catalyst behaviour. This has been recently shown e.g. for Co/Al_2O_3 Fischer Tropsch catalysts [7] and for Ni-Mo sulphide HDS catalysts [8].

NiO/Al_2O_3 materials may have interest for their own catalytic activity [9-13], but are mostly synthesized industrially as precursors of Ni/Al_2O_3 based supported metal catalysts for methanation [14,15] and other hydrogenation reactions [16] and for steam reforming and pre-reforming of natural gas [17], propane [18], ethanol [19,20], biomass tar [21,22] and bio-oils [20,23], In previous studies we reported the characterization of Ni/Al_2O_3 catalysts prepared with a silica-containing support and calcined (after impregnation) at 700 °C [24,25]. In the present paper we will address the effect of silica addition and of the calcination temperature on the properties of Ni/Al_2O_3 catalysts we apply to steam reforming and hydrogenation reactions.

2. Experimental

2.1 Materials preparation

Two alumina-based materials, Puralox Sba 200 ("pure" Al_2O_3) and Siralox 5/170 (5% SiO_2 and 95% Al_2O_3), both produced by Sasol, were used as received (hereinafter denoted as P and S sample, respectively) or stabilized at 1073 K for 5 hours (P800 and S800) as catalysts supports.

Nickel addition at different loadings 5%, 16% and 39% ($w_{Ni}/w_{support}$) on S, P, S800 and P800 were performed through wet impregnation of an aqueous solution of $Ni(NO_3)_2*6H_2O$. A step of drying at 363 K for 5 hours was then performed and the samples were finally calcined at 973 K (xNiP700 and xNiS700) and 1073 K (xNiP800 and xNiS800) respectively in order to obtain the catalyst in the oxide form.

2.2 Materials characterization

Surface area measurements were done with the single point method in a volumetric line after outgassing at 473 K for 30 minutes in vacuum.

X-Ray diffraction patterns were recorded using Cu Kα radiation (λ=0.15406 nm). XRD analysis of the samples were obtained using a vertical powder diffractometer X'Pert. The patterns were collected in the 25 – 100° 2θ range with a step of 0.02° and a counting time for each step in-between 9-20 s depending on the Ni loading. Powder patterns were indexed by comparing experimental results to the data reported in the Pearson's Crystal Data [26] and JCPDS-ICDD databases [27].

Skeletal IR spectra where recorded using KBr pressed disks (weight 0.808 g) and a Nicolet Nexus instrument (OMNIC software, DTGS detector, 100 scans). All the spectra are reported in common scale. UV-vis-NIR spectra were collected on pure powder with a JASCO V570 instrument.

H_2-temperature-programmed-reduction (H_2-TPR) experiments were carried out at atmospheric pressure in a tubular flow reactor using a fixed bed containing a mixture of 150 mg of catalyst and 500 mg of sand (50-70 mesh sieved, Sigma-Aldrich, calcined at 1073 K for 6 h). The catalyst was pretreated at 773 K for 1h flowing 50 cc/min of nitrogen and then it was cooled down in nitrogen. TPR was performed under N_2-H_2 mixture flow (80 cc/min, 89%N_2 and 11%H_2) with temperature increasing from room temperature (RT) to

1173 K at the heating rate of 10 K/min. TPR profiles were recorded by analysing the outlet flow with a Nicolet 380 FT-IR spectrometer acquiring a complete series in the 4000-400 cm^{-1} mid infrared range with 4 scans and a resolution of 2 cm^{-1}. The absorbance of the peak at 1540 cm^{-1} (roto-vibrational component of the H-O-H bending mode of water vapour) was used to determine water outlet concentration. The obtained signal was smoothed in order to have a reliable comparison between the different signals. The pipeline connecting the line and the IR cell was constantly heated at 308 K in order to avoid water condensation.

A Scanning Electron Microscope (SEM) Zeiss SUPRA 40 VP microscope, equipped with a field emission gun was used to investigate sample morphology. This instrument is equipped with a high sensitivity “InLens” secondary electron detector and with a EDX microanalysis OXFORD "INCA Energie 450x3". Samples were suspended in ethanol under ultrasonic vibrations to decrease particle aggregation. A drop of the resultant mixture was deposited on a Lacey Carbon copper grid and the dried sample was then imaged.

2.3 Catalytic experiments

A tubular quartz flow reactor, containing a fixed bed with 88.0 mg of catalyst mixed with 440 mg of quartz particles 0.25–0.21 mm (corresponding to 60-70 mesh sieved) was used in steady-state catalytic experiments. The total gas flow-rate was 80 Nml/min with the following composition 4% ethanol, 24% water and 72% He as carrier gas, giving a gas hourly space velocity GHSV equal to 55000 h^{-1} (NTP). In order to follow any hysteresis or deactivation effects, experiments were performed both in ascending and descending reaction temperature (523K, 673K, 773K, 873 K, 973 K, 1023 K and reverse).
Product analysis was performed with a gas-chromatograph Agilent 4890 equipped with a Varian capillary column “Molsieve 5A/Porabond Q Tandem” and TCD and FID detectors in series. Between them a Nickel Catalyst Tube was employed to reduce CO and CO_2 to CH_4. Products analysis in the first case was also performed with a GC/MS (ThermoFisher), in order to have a precise identification of the involved compounds.

Reactants conversion is defined as follows:

$$(1)\quad X_{\text{reactant}} = \frac{n_{\text{react.in}} - n_{\text{react.out}}}{n_{\text{react.in}}}$$

while selectivity to product *i* is defined as follows:

$$(2)\quad S_i = \frac{n_i}{\nu_i(n_{EtOH\ in} - n_{EtOH\ out})}$$

where n_i is the moles number of compound i, and ν_i is the ratio of stoichiometric reaction coefficients. Hydrogen yield was defined for ESR experiments as:

$$(3)\ Y_{H2} = \frac{n_{H2}}{\nu_i n_{EtOH\ in}}$$

3. Results

3.1 IR study of the starting supports.

The starting supports Puralox (P) and Siralox (S) have been characterized by IR spectroscopy. The IR spectra in the region of the OH stretching of the surface hydroxyl groups, recorded after outgassing at 773 K, are presented in Fig. 1,A. The spectrum of P shows the main bands at 3794, 3767, 3725 and ca 3680 cm^{-1}, typical of the surface OHs of γ-Al_2O_3, as discussed elsewhere [5,6]. The spectrum of S shows a prominent sharp band at 3735 cm^{-1}, assigned to OH stretching of the silanol group. The highest frequency band is shifted down to 3787 cm^{-1} while the strong band observed for P at 3767 cm^{-1} vanished. The component at 3726 cm^{-1} is present as a shoulder of the silanol band, while at lower frequency the spectrum of S presents a broader absorption than that observed for P. It is evident that the addition of silica perturbed significantly and somehow selectively the spectrum of the surface OH's of alumina. In Fig. 1,B the IR spectra of residual CO species, adsorbed after contact with CO at 140 K followed by outgassing upon warming up to 190 K, are reported. On sample P a band constituted by two components at 2218 and 2207 cm^{-1} is observed, while on S the component at 2218 cm^{-1} is almost disappeared and that at 2207 cm^{-1} is present, weaker.

Fig. 1,C shows the IR subtraction spectra of residual adsorbed pyridine after outgassing at 298 K. Pyridine adsorbed on P gives rise to three 8a components observed at 1597, 1614 and 1621 cm^{-1}, corresponding to a complex 19b band centered at 1447 cm^{-1} with a prominent component at 1456 cm^{-1}, revealing the existence of at least three different families of Lewis acid sites as typical of γ-Al_2O_3. The spectrum of S is closely similar, but the shoulders at 1621 and 1456 cm^{-1} are definitely less pronounced than in the spectrum of P.

The spectra of adsorbed CO and pyridine confirm that the addition of silica decreases the amounts of Lewis acid sites killing most of the strongest ones, leaving almost unaltered the others.

3.2 XRD study.

In Figs. 2 and 3 the XRD patterns of the samples under study are reported. The patterns reveal that the Si-free starting alumina material (Puralox, P) consists of cubic γ-Al_2O_3, JCPDS table 75-0921, Fig. 2. After calcination at 1073 K (P800) the XRD pattern is slightly different: the more evident complexity in the 2θ range 30° ÷ 40° and the partial resolution of two components in the peaks near $2\theta \sim 46°$ and ~ 67° (400 and 440 spinel peaks, respectively) can be taken as an evidence of a tetragonally distorted defective spinel alumina similar to δ-Al_2O_3, JCPDS card 088-1609 [28], or γ'-Al_2O_3 [29].

The XRD pattern of the starting Siralox support (S, Fig. 3) does not change upon calcination at 1073 K (S800), and is similar to that of P800, thus being assigned to tetragonally distorted defective spinel alumina similar to δ-Al_2O_3.

The addition of 5% Ni at the surface of Puralox does not modify significantly the XRD patterns neither of P (γ-Al_2O_3) nor of P800 (δ-Al_2O_3). At higher Ni loadings, two types of modifications of the XRD pattern are observed: 1) the appearance of the XRD peaks of the NiO (bunsenite) phase (rock salt type); 2) the modification of the spectrum of alumina with significant shifts to lower angles of the two most intense 440 and 400 spinel peaks and the growth in intensity of the 511 and, in particular, of the 311 spinel peaks, $2\theta \sim 56°$ and $2\theta \sim 37°$, with respect to all others, and the corresponding disappearance of the 222 peak, $2\theta \sim 40°$, showing the progressive formation of a XRD pattern similar to that of $NiAl_2O_4$ spinel phase [30,31]. The spectra of the XNiP700 series actually correspond to the pattern of γ-Al_2O_3, to which that of NiO is superimposed only in the case of the 39NiP700 sample. Instead in the case of the XNiP800 series the pattern of δ-Al_2O_3 of the Ni-free parent material is progressively modified towards that of $NiAl_2O_4$ in all cases, while the pattern of NiO additionally appears only in the case of 39NiP800.

In the case of the XNiS700 series, the pattern of δ-Al_2O_3 is also observed over which the features of NiO appear already in the case of the 16NiS700 sample and further grow in the case of the 39NiS700 sample. In the case of the XNiS800 series, the spectrum modifies to

that of $NiAl_2O_4$ with only negligible amounts of NiO in the case of 16NiS800, while the pattern of NiO is well evident only for 39NiS800.

3.3 Skeletal IR spectra.

In Fig. 4 the infrared skeletal spectra of the materials are reported. The spectra of the samples P and 5NiP700 confirm the results obtained by XRD, showing the typical broad poorly resolved features of γ-Al_2O_3 [5,6]. In the spectra of 16NiP700 and 39NiP700 the background due to γ-Al_2O_3 is superimposed by other absorptions centred near 505 cm^{-1} with a shoulder at 470 cm^{-1} and a more pronounced component at 725 cm^{-1}. The modes at 725 and 505 cm^{-1} are associated to the most intense IR active modes of the $NiAl_2O_4$ spinel [30,31,32] while that at 470 cm^{-1} nearly corresponds to the TO mode of the only IR active mode of nano-crystalline NiO [24]. Also the spectra of P800 and 5NiP800 confirm the results obtained by XRD, showing sharper features superimposed on the main absorption, typical of the spectrum of δ-Al_2O_3 [5,6]. As for the XNiP800 series, the modification of the IR spectrum by increasing Ni loading is more evident, with the appearance of two strong bands at ca 500 and ca 740 cm^{-1}, with a further shoulder near 830 cm^{-1}, typical of the $NiAl_2O_4$ spinel but also similar to that of cationically deficient $Ni_xAl_2O_{3+x}$ spinels [30]. However, by comparing the spectra of 16NiP800 (for which the XRD show only the spectra of a Ni aluminate) and of 39NiP800 (for which XRD also shows the formation of NiO) the difference is just for the presence, in the case of 39NiP800, of an evident shoulder near 470 cm^{-1} that can be assigned to NiO, as above. The spectra of XNiS800 series are similar to those of the XNiP800 series, showing again the formation of the spectrum of the aluminate spinel. However the spectrum of the Ni aluminate phase is very evident only for 39NiS800 while that of 16NiS800 seems more to be an intermediate one between alumina and aluminate. The spectra of the 5NiS700 and 16NiS700 samples are similar to those of the starting δ-Al_2O_3 support, while that of 16NiP800 is very close to that of $Ni_xAl_2O_{3+x}$ spinels [30] and that of 39NiP800 is similar but with a more pronounced component near 470 cm^{-1} due to NiO.

3.4 UV-vis spectroscopic characterization

The diffuse reflectance UV-visible and Near Infrared spectra (DR-UV-vis-NIR) of the catalysts are reported in Figs. 5 and 6. The pure alumina supports do not show any evident absorption at the scale used in the figures. In contrast, the Nickel containing samples spectra show absorptions in the visible-NIR region as well as in the UV region.

In the spectra of the samples with low Ni content (5NiPs and 5NiSs) an absorption tail is observed in the UV range 240-300 nm (Fig. 4) which is likely the higher wavelength side of an absorption associated to a O^{2-} (2p) $\rightarrow$ Ni^{2+} (3d) charge transfer transition (CT). In any case the spectra are almost identical with each other and similar to those reported previously and assigned to "isolated" Ni^{2+} species dispersed on alumina [24,25].

The spectra of the 16NiPs in the UV region are much more intense but qualitatively similar, not showing a definite maximum for this absorption in the region above 220 nm, but only an absorption tail whose intensity decreases by increasing wavelength. In the case of the 16NiSs samples, instead, the absorption seems to have a different shape with a well-defined shoulder near 300 nm in the case of 16NiS800 and the same shoulder with an additional maximum at 260 nm in the case of 16NiS700. The shift of the maximum of the O^{2-} (2p) $\rightarrow$ Ni^{2+} (3d) CT transition to higher wavelength is an effect of increasing Ni loading and of the change of support from P to S. Thus, it could be associated to an increased vicinity of the Ni^{2+} ions, which could be less "dispersed" (thus become nearer each other) on S than on P supports. In practice, the lowered energy of the CT transition can be due to the increased superposition of the orbitals of Ni^{2+}, converting from localized orbitals to bands.

For the most charged samples 39Nis, the absorption in the UV range shows two main maxima, near 260 and 300 nm, which look quite similar to those observed for $NiAl_2O_4$ [33]. Only in the case of the 39NiP800 sample the component at 300 nm is much weaker than that at 260 nm, suggesting that the main $NiAl_2O_4$ –like absorptions are superimposed on the tail associated to the absorption of isolated Ni^{2+} ions.

As for comparison, we can compare the observed spectra with that recorded for bulk NiO nanoparticles, that shows the O^{2-} (2p) $\rightarrow$ Ni^{2+} (3d) CT transition similar to an absorption plateau with two predominant components at 240 and 330 nm, the last sharp. This feature (found previously in the case of very heavily charged NiS samples [24]), might be present in the spectra of 39Nis samples, as well as in the of the 16NiS700 sample, superimposed to the main $NiAl_2O_4$ –like absorptions, but is not present in the others.

Summarizing, the trend of the main absorption can be used to determine some difference between the state of Ni^{2+} ions. We can conclude that at least three different spectra can be found in the UV region identifying three different Ni^{2+} species: NiO particles, $NiAl_2O_4$ –like structures and highly dispersed Ni^{2+}.

The absorptions observed in the spectra of the Ni-containing samples above 350 nm are associated to the d $\rightarrow$ d transitions of Ni^{2+}. Low Ni-content samples (5Ni) show a sharp

doublet at 595-8 and 625-9 nm and a broad absorption in the NIR centred at 1000-1020 nm. Interestingly, the latter absorption is definitely centred at higher wavelength on NiS samples than on NiP samples, both for 5Ni and for 16Ni samples. These absorptions in the visible-NIR regions are for their shape and position similar to those reported for $NiAl_2O_4$ [33]. By increasing Ni content the absorption in the NIR shifts to higher wavelength apparently due to the growth of a component located near 1120 nm. In the case of the samples with 39Nis a sharp maximum grows at 718 nm, typical of NiO.

The features associated to NiO nanoparticles are still essentially absent (extremely weak traces if any) in the case of 16NiP700, 16NiP800 and 16NiS800 but very weak also for 39NiP800. In contrast, these features are well pronounced for 39NiP700 and 39NiS800. Finally, the features of NiO are very intense (e.g. the peak 718 nm is definitely more intense than that at ca 640 nm) only in the case of 39NiS700, where XRD show the maximum amount of NiO. On the other hand, the behaviour of the band in the NIR region suggests that in low loading sample (Ni5 in particular) Ni^{2+} ions interact each other more on S than on P samples, being shifted down on S samples as on NiO.

3.5 TPR study.

The TPR profiles of the samples are compared in Fig. 7. The profiles of Ni5Ps and Ni5Ss samples show a simple reduction peak with a maximum at ca. 1123 K, except for 5NiS800, whose maximum is at even higher temperature. This peak is associated to Ni^{2+} highly dispersed and very resistant to reduction. The samples with 16% Ni present also this peak but shifted at a slightly lower temperature, and, except for 5NiP800, an additional component at lower temperature. In fact, the TPR profile of 16NiP800 shows an additional broad and weak component centred near 800 K, that of 16NiP700 shows the main peak definitely broad with a minor component near 1000 K while that of 16P800 shows a pronounced but weak shoulder at ca 950 K. In the case of the TPR prfiles of the samples with 39% Ni, the lower temperature component at ca 800 K is always present, definitely more pronounced. Only in the case of 39NiS700 a third pronounced component at ca 600 K is found, attributed to the reduction of unsupported NiO particles, in agreement with the literature [34-37]. As discussed previously [25], the comparison of TPR with XRD data shows that two kinds of NiO really exist, one of which behave as bulk NiO, while the other is less easily reducible.

3.6 FE-SEM study.

In Figs. 8 and 9 the FE-SEM micrographs of some samples are reported. The figures recorded by an InLens detector for secondary electrons are compared with those recorded using the solid state back-scattered electrons (BSE) detector, in order to take advantage of the compositional contrast to look at the Ni dispersion. The samples containing 5 and 16 % Ni show a good dispersion of the Ni species, associated to diffused and homogeneous brightness on the alumina particle in the BSE image. This is shown in Fig 8 up, for 5NiS800. In the case of the sample 16NiS800 few very small Ni-rich particles are evident (see Fig. 8, down). The size of these particles is 10 nm or less. In agreement , this sample shows only broad extremely weak features due to NiO peaks to XRD analysis. More evident NiO particles are observed in the FESEM images of 16NiS700 which in fact shows definite NiO features both in XRD pattern and in the visible-NIR spectra. In contrast, samples loaded with 39% Ni all show well evident Ni-rich particles with 50-100 nm diameter. However the samples produced with Puralox support are almost perfect hexagonal platelets as shown in Fig. 8 up for 39NiP700, while those prepared with the Siralox support are in part globular and in part hexagonal, but less well defined.

3.7 Catalytic activity in Ethanol Steam Reforming (ESR).

In tables 2-5 the data on the catalytic activity of the samples in ethanol steam reforming (ESR) are summarized. The experiments are performed with increasing temperature steps, without any previous pretreatment. The samples 39NiP800 gives rise to excellent ESR activity at 873 K with a 87 % hydrogen yield. The sample 39NiS700 is even more efficient giving rise to 88% hydrogen yield at 773K. The 16NiS700 catalyst instead gives good ESR activity only at 1023 K. On the other hand, it is evident that the sample 16NiP800 does not show good ESR activity. In fact it gives rise mainly to ethanol dehydration to DEE and ethylene (98% yield to ethylene at 773 K) while at even higher temperature some ethanol decomposition to CH_4 + CO is also observed.

4. Discussion

The surface area measurements show that the starting Si-free Puralox sample has a slightly higher surface area of the starting Si-containing Siralox sample. This might be due to some pore blocking during the preparation of Siralox. However, when the two samples

are calcined at 800 °C (1073 K), Siralox retains a higher surface area than Puralox, confirming the well-known stabilizing effect of silica against alumina sintering. In all cases increasing Ni loading results in a significant decrease of surface area, very limited when 5% Ni only is present, but more significant for 16%Ni loading and even more for 39% Ni loading. This effect is more pronounced in the case of Siralox than of Puralox samples, although the corresponding Ni-containing samples retain higher surface area if supported on Siralox than on Puralox when calcined at 1073 K. This would confirm that the use of a silica-containing alumina support can help in retaining high surface area at high temperature.

XRD pattern of the starting Puralox sample is typical for cubic γ-Al_2O_3 but converts into that typical for tetragonally distorted δ-Al_2O_3 or γ'-Al_2O_3 by calcination at 1073 K. Instead the starting Siralox sample shows the XRD pattern typical for tetragonally distorted δ-Al_2O_3 or γ'-Al_2O_3 which is retained after calcination at 1073 K. In some way, the presence of silica could favor the evolution of the cubic defective spinel into a tetragonally distorted defective spinel.

The all data show that all samples loaded with 5 % Ni give rise to well dispersed Ni^{2+} species. This is evident when FESE microscopies are analyzed, where Ni-rich particles are not observed. Interestingly, the XRD pattern of the 5NiP700 sample retains the feature of cubic γ-Al_2O_3 while in the other cases the XRD typical for tetragonally distorted δ-Al_2O_3 or γ'-Al_2O_3 is retained. The UV spectrum of these samples shows a tail with increasing absorption upon lowering wavelength, suggesting that the $O^{2-} \rightarrow Ni^{2+}$ CT transition for this species falls below 220 nm, the lower λ limit in our measurements. Besides a weak absorption at 370 nm, the spectra show in the visible region a doublet at 600 and 633 nm, and in the NIR region a broad maximum near 1000 nm. These absorptions would be due to the d$\rightarrow$d transitions of "isolated" Ni^{2+}. The position of the band in the NIR region might suggest that Ni^{2+} species interact more each other (thus being nearer) on S than on P support. The skeletal IR spectrum of these samples is similar to that of cubic γ-Al_2O_3 for 5NiP700 and of tetragonally distorted δ-Al_2O_3 or γ'-Al_2O_3 for the other samples with 5 % Ni. Thus, the mentioned features are assigned to well dispersed Ni^{2+} on spinel-like alumina support. TPR curves show that these species are reduced only at very high temperatures, near 1200 K. These samples show very low ESR activity (not reported here).

The samples with loaded 16% Ni, instead, show some significant differences depending on the support and on the calcination temperature. The XRD pattern of 16NiP700 is still that of the γ-Al_2O_3 support, while that of 16NiP800 shows a definite modification towards that of $NiAl_2O_4$ spinel, with respect to that of the P800 support which is typical of tetragonally distorted δ-Al_2O_3 or γ'-Al_2O_3. The XRD pattern of 16NiS700 is similar to that of the support (typical of tetragonally distorted δ-Al_2O_3 or γ'-Al_2O_3) but with the addition of small peaks due to NiO. Instead, XRD pattern of 16NiS800 does not show the features of NiO (or, better, show them extremely weak) but shows the alumina features only very slightly evolved towards the $NiAl_2O_4$ spinel pattern. The skeletal IR spectra confirm the XRD data, being typical for $NiAl_2O_4$ in the case of 16NiP800, similar to that of the tetragonally distorted δ-Al_2O_3 or γ'-Al_2O_3 for 16NiS700 and 16NiS800, and essentially intermediate between those of γ-Al_2O_3 and $NiAl_2O_4$ for 16NiP700. FESEM images confirm the good dispersion of Ni^{2+} in these cases and the presence of very small NiO particles in the case of 16NiS800 and bigger ones in the case of 16NiS700. Also the visible spectra show the presence of NiO in the sample 16NiS700: in fact a well-defined peak is found at 715 nm, observed also for NiO nanoparticles. Additionally, the broad band in the NIR region is centered now near 1150 cm^{-1}, i.e. near the value found for NiO. However, these features in the electronic spectra are observed, very weak, also for Ni16S800 and Ni16P800, suggesting that very few and small NiO particles can also be present in these cases. The UV spectra for these samples still do not show a definite maximum, but only a tail in the region for λ > 220 nm. The shape of the absorption in the UV suggest that also "dispersed" Ni^{2+} ions interact each other more on S than on P support. TPR curves still show an only peak centered near 1100 K, but with broad weak features at lower temperature, larger on S than on P support.

In the particular case of the sample 16NiP800, the characterization results (XRD and IR) indicate that a Ni alumina spinel is formed. We can mention that the chemical composition of the sample is corresponding to the formula $Ni_{0.28}Al_2O_{3,28}$, i.e. a still largely deficient spinel. On the other hand, the spectroscopic features of this sample well correspond to those previously reported for a $Ni_{0.5}Al_2O_{3,5}$ cationic deficient spinel, which are also very similar to those of stoichiometric $NiAl_2O_4$ [30].

In the case of the samples loaded with 39% Ni the presence of NiO is evident in all cases to XRD. However, samples with Puralox support have relatively less NiO than samples with Siralox support. 39NiS700 has the maximum NiO content, according to XRD, vis

spectroscopy and IR spectroscopy. Accordingly, it is also the only sample that shows a peak near 600 K in the TPR curve, typical of reduction of bulk NiO.

Catalytic data show that samples characterized (when fresh) by the presence of NiO particles have excellent activity in the ESR reaction at 873 K. The sample richest in NiO, 39NiS700 gives rise to excellent ESR activity already at 773 K. On the other hand, this is the only sample that shows in the TPR experiments the reduction peak of NiO particles centered at 650 K, but the NiO reduction threshold below 773 K. Thus, this is the only sample where reduction of NiO to Ni is already occurring at 773 K. Previous studies showed that the formation of Ni metal particles by NiO particles reduction is essential for good catalytic activity in Ni-Al based catalysts [38,39,40]. On the other hand, the sample 16NiP800, where Ni is largely and essentially in the form of a Ni aluminate, has very low catalytic activity in ESR only above 1000 K. TPR shows that in this case Ni reduction starts above 1000 K.

The overall data discussed here show that the presence of 5% silica in the alumina supports modify considerably the ability of the alumina support to disperse Ni oxide species. The above 5NiP700 sample contains about 2.5 Ni atoms per nm^2 of alumina surface. Similarly, also the starting Siralox sample contains nearly 2.5 silicate units per nm^2. Taking into account that an atomic unit may cover something less than 0.1 nm^2 the fractional geometric coverage of the alumina support is in both cases less than 0.25 at most. The higher loading 16NiP700 and 39NiP700 samples contain ~ 8.2 and ~ 20 at_{Ni}/nm^2_{Al2O3}, respectively, that could nearly correspond to 80% of a monolayer and two monolayers, respectively.

The additional presence of 5% silica seems to produce Ni^{2+} species which interact each other more than on silica-free alumina. When the Ni loading approaches that can be sufficient to produce a “monolayer” (as for the 16Ni samples), the effect of silica is to hinder the dispersion of Ni^{2+} ions and to favor the formation of NiO. This is also evident on samples containing 39% Ni, where the amount of NiO formed is larger on S than on P supported catalyst.

As for catalysts calcined at 1073 K, the presence of silica clearly hinders the formation of Ni aluminate, again favoring the formation of NiO.

This suggests that Ni^{2+} ions preferentially anchor on a limited number of “active sites” on the alumina surface, which become somehow “poisoned” by silica on the Siralox support. Dispersed Ni^{2+} species stay essentially as supported species in the case of samples

calcined at 973 K but penetrate at least in part onto alumina forming Ni-aluminate-like structure when calcined at 1073 K.

The number of the alumina's "active sites" to which Ni^{2+} cations anchor preferentially is of the order of 2,5 sites/nm^2 or less, that is larger of the same order of magnitude of the number of residual OH groups usually measured for alumina after outgassing at "normal" temperatures (e.g. 773 K). In fact, IR spectra shows that the 5% silica present in Siralox strongly modifies the spectrum of the surface OH's and kills preferentially some of them (e.g. those absorbing at 3787 cm^{-1}). Similarly, also the strongest Lewis acid sites (νCO at 2218 cm^{-1} and ν8a of adsorbed pyridine at 1622 cm^{-1}) are significantly decreased in the case of Siralox with respect to Puralox. Accordingly, it has been previously observed that Siralox has lower catalytic activity than Puralox in the dehydration of ethanol [41].

These data support the idea that most of the surface chemistry of alumina takes place on a limited number of defects, likely including edges and corners of the nanocrystals, more than on extended surfaces. This confirms that modeling of surface defects is far more important that modeling of surface faces, to understand the surface chemistry of alumina. This result can be extended to the study of the phenomena occurring during the preparation of alumina supported catalysts, i.e. supported metallic catalysts and supported sulphide catalysts.

5. Conclusions.

1. It is confirmed that small amounts of silica hinder the surface area loss of alumina upon calcination, allowing the retention of higher surface areas also when NiO is deposed on the support.

2. If calcination is performed at 973 K in the absence of silica, nickel impregnation on γ-Al_2O_3 gives rise to a "layer" of dispersed Ni^{2+} on γ-Al_2O_3 for 5% and 16 % Ni loading, while for 39% Ni loading, NiO forms on γ-Al_2O_3.

3. If calcination is performed at 1073 K in the absence of silica, nickel impregnation on δ-Al_2O_3 or γ'-Al_2O_3 gives rise to the progressive formation of a defective $Ni_xAl_2O_{3+x}$ aluminate spinel phase for 5 and 16 % impregnated Ni, while for 39% impregnated Ni, NiO particles form over a deficient Ni-aluminate type phase.

4. The presence of 5% silica hinders the formation of Ni aluminate phase, and favors the formation of NiO phase. This is attributed to the competition of silica and nickel oxide for interaction on the most reactive surface sites of alumina. Silica shifts Ni species to less reactive sites where the Ni-Alumina interaction is weaker.

5. As a result of this, the addition of silica to alumina support gives rise to more easily reducible Ni catalysts, that become active in ESR at lower temperature.

6. It is further supported the idea that the surface chemistry of alumina takes mostly place on a limited number of defects, likely including edges and corners of the nanocrystals, more than on extended surfaces.

Table 1: Composition, surface area of the analysed materials

Notation	Support	calcination T [°C]	%SiO_2 (w_{SiO2}/w)	%Ni ($w_{Ni}/w_{support}$)	BET [m^2/g]
P	Puralox	as received	0	0	198
5NiP700	Puralox	700	0	5	165
16NiP700	Puralox	700	0	16	157
39NiP700	Puralox	700	0	39	120
P800	Puralox	800	0	0	107
5NiP800	Puralox	800	0	5	104
16NiP800	Puralox	800	0	16	96
39NiP800	Puralox	800	0	39	80
S	Siralox	as received	5	0	170
5NiS700	Siralox	700	5	5	165
16NiS700	Siralox	700	5	16	137
39NiS700	Siralox	700	5	39	107
S800	Siralox	800	5	0	142
5NiS800	Siralox	800	5	5	136
16NiS800	Siralox	800	5	16	110
39NiS800	Siralox	800	5	39	92

Eliminato: Interruzione di sezione (pagina successiva)

Table 2: ESR results on Ni16S700 in terms of conversions (X_i), H_2 yield (Y_{H2}) and selectivities (S_i) towards C-compounds.

T furnace [K]	X C_2H_5OH	X H_2O	Y H_2	S CH_4	S CO	S CO_2	S C_2H_4	S C_2H_6	S C_3H_6	S C_2H_4O	S $C_4H_{10}O$	S $C_4H_8O_2$
523	0.00	0.00	0.00	0.00	0.00	0.00	0.00	0.00	0.00	0.00	1.00	0.00
573	0.06	0.00	0.00	0.00	0.01	0.03	0.09	0.00	0.00	0.18	0.69	0.01
673	0.59	-0.07	0.02	0.00	0.00	0.00	0.56	0.00	0.00	0.18	0.25	0.01
773	1.00	-0.12	0.10	0.00	0.01	0.02	0.72	0.01	0.02	0.19	0.02	0.00
873	1.00	-0.09	0.10	0.04	0.05	0.08	0.66	0.01	0.05	0.04	0.08	0.00
973	1.00	0.03	0.32	0.09	0.33	0.13	0.40	0.04	0.01	0.00	0.00	0.00
1023	1.00	0.37	0.87	0.00	0.38	0.62	0.00	0.00	0.00	0.00	0.00	0.00

Table 3: ESR results on Ni39S700 in terms of conversions (X_i), H_2 yield (Y_{H2}) and selectivities (S_i) towards C-compounds.

T furnace [K]	X C_2H_5OH	X H_2O	Y H_2	S CH_4	S CO	S CO_2	S C_2H_4	S C_2H_6	S C_2H_4O	S $C_4H_{10}O$	S $C_4H_8O_2$	S C_3H_6O
523	0.01	0.00	0.00	0.00	0.00	0.00	0.00	0.00	0.00	1.00	0.00	0.00
573	0.05	0.00	0.00	0.00	0.00	0.03	0.06	0.00	0.30	0.61	0.00	0.00
673	0.44	-0.04	0.02	0.00	0.00	0.00	0.37	0.01	0.25	0.36	0.01	0.01
773	1.00	0.43	0.88	0.07	0.07	0.86	0.00	0.00	0.00	0.00	0.00	0.00

Table 4: ESR results on Ni39P800 in terms of conversions (X_i), H_2 yield (Y_{H2}) and selectivities (S_i) towards C-compounds.

T furnace [K]	X C_2H_5OH	X H_2O	Y H_2	S CH_4	S CO	S CO_2	S C_2H_4	S C_2H_6	S C_3H_6	S C_2H_4O	S $C_4H_{10}O$	S C_3H_6O
523	0.02	0.00	0.00	0.00	0.00	0.00	0.00	0.00	0.00	0.00	1.00	0.00
573	0.25	-0.02	0.00	0.00	0.00	0.00	0.19	0.00	0.00	0.02	0.79	0.00
673	0.73	-0.11	0.01	0.00	0.00	0.00	0.81	0.03	0.00	0.05	0.10	0.00
773	1.00	-0.14	0.03	0.00	0.00	0.02	0.87	0.00	0.01	0.06	0.00	0.03
873	1.00	0.39	0.87	0.02	0.29	0.69	0.00	0.00	0.00	0.00	0.00	0.00
973	1.00	0.39	0.89	0.00	0.34	0.66	0.00	0.00	0.00	0.00	0.00	0.00
1073	1.00	0.37	0.87	0.00	0.37	0.62	0.00	0.01	0.00	0.00	0.00	0.00

Figure captions

Figure 1. A) IR spectra for the OH stretching region of the surface hydroxyl groups, recorded after outgassing at 773 K. B) IR spectra of residual CO species after contact with CO at 140 K and successive outgassing and warming up to 190 K. C) IR subtraction spectra of residual adsorbed pyridine on S and P after outgassing at 298 K.

Figure 2. XRD diffraction patterns of P, P800, XNiP700 and XNiP800. The following compounds were indexed • NiO, ◊$NiAl_2O_4$ or γ-Al_2O_3.

Figure 3. XRD diffraction patterns of S, S800, XNiS700 and XNiS800. The following compounds were indexed • NiO and ◊$NiAl_2O_4$

Figure 4. Skeletal IR spectra of all the catalyst under investigation.

Figure 5. Diffuse reflectance UV of all the investigated catalysts together with the spectrum of NiO. All the spectra are reported in common scale.

Figure 6. Diffuse reflectance vis-NIR spectra of all the investigated catalyst in common scale.

Figure 7. H_2-TPR profiles of all the investigated samples following the signal at 1540 cm-1 of vapour water produced by the metal reduction.

Figure 8. FE-SEM micrographs acquired respectively with Inlens (SE) detector and SSD (BSE) detector of 5NiP800 (top) and 16NiS800 (bottom)

Figure 9. FE-SEM micrographs acquired respectively with Inlens (SE) detector and SSD (BSE) detector of 39NiP700 (top) and 39NiS700 (bottom)

References

[1] G. Busca, Heterogeneous Catalytic Materials, Elsevier, 2014, pp. 375-419.

[2] J. A. Anderson, M.Fernández García (eds.), Supported Metals in Catalysis, Imperial College Press, London, 2011.

[3] P. Raybaud, H. Toulhoat (eds.), Catalysis by Transition Metal Sulphides, from Molecular Theory to Industrial Application, Editions Rechnip, 2013

[4] L. Lietti, P. Forzatti, G. Ramis, G. Busca, F. Bregani, Appl. Catal. B: Envir., 3 (1993) 13-35.

[5] G. Busca, Catal. Today, 226 (2014) 2-13.

[6] G. Busca, Advan. Catal., 57 (2014) 319-404

[7] A. Jean-Marie, A. Griboval-Constant, A.Y. Khodakov, F. Deiehl, C.R. Chimie 12 (2009) 660-667.

[8] J. Ramirez, F. Sanchez-Minero, Catal. Today 130 (2008) 267-271.

[9] H. Zhu, S. Ould-Chikh, D. H. Anjum, M. Sun, G. Biausque, J.M. Basset, V. Caps, J. Catal. 285 (2012) 292-303

[10] F. Patcas, F.C. Patcas, Catal. Today 117 (2006) 253-258

[11] S. Nassos, E. Elm Svensson, M. Boutonnet, S.G. Järås, Appl. Cat. B: Env. 74 (2007), 92-102

[12] M. Stoyanova, P. Konova, P. Nikolov, A. Naydenov, St. Christoskova, D. Mehandjiev Ch. Eng. J. 122 (2006), 41-46

[13] C. Dueso, M. Ortiz, A. Abad, F. García-Labiano, L. F. de Diego, P. Gayán, J. Adánez Ch. Eng. J. 188 (2012), 142-154

[14] J.R. Røstrup-Nielsen , K. Pedersen, J. Sehested, Appl. Catal. A: Gen. 330 (2007) 134-138.

[15] J. Kopyscinski, T.J. Schildhauer, S.M.A. Biollaz, Fuel 89 (2010) 1763-1783.

[16] http://www.jmcatalysts.com

[17] J. Sehested, Catal. Today 111 (2006) 103–110.

[18] S. Nathesakawat, R.B. Watson, X.Q. Wang, U.S. Ozkan, J. Mol. Catal. A: Chem. 241 (2005) 133-146.

[19] J. Sun, Y. Wang, ACS Catal. 4 (2014) 1078–1090.

[20] G. Nahar, V. Dupont, Biofuels 3 (2012) 167-191.

[21] F. Basile, S. Albertazzi, D. Barbera, P. Benito, J. Einvall, J. Brandin, G. Fornasari, F. Trifirò, A. Vaccari, Biomass Bioen. 35 (2011) S116 -S122.

[22] F.L. Chan, A. Tanksale, Renew. Sust. Energ. Rev. 38 (2014) 428–438.

[23] E.C. Vagia, A.A. Lemonidou, Appl. Catal. A: Gen. 351 (2008) 111–121.

[24] G. Garbarino, S. Campodonico, A. Romero Perez, M. M. Carnasciali, P. Riani, E. Finocchio, G. Busca, Appl. Catal. A: Gen., 452 (2013) 163-173

[25] G. Garbarino, I. Valsamakis, P. Riani, G. Busca, Cat. Comm., 51 (2014) 37-41.

[26] “Pearson Crystal Data: Crystal structure database for inorganic compounds”, Release 2009/2012, ASM International, The Material Information Society

[27] http://www.icdd.com/

[28] L. Kovarik, M.Bowden, A. Genc, J.Szanyi, C.H.F. Peden, Ja H. Kwak, J. Phys. Chem. C, 2014, 118 (31), pp 18051–18058

[29] G. Paglia, C.E. Buckey, A.L. Rohl, R.D. Hart, k. Winter, A. J. Studer, B.A. Hunter, J.V. Hanna, Chem. Mater., 2004, 16, 220-236

[30] G. Busca, V. Lorenzelli, V. Sanchez Escribano, Chem. Mater. 4 (1992) 595-605.

[31] R. Samkaria, V.Sharm, Mater. Sci. Eng. B 178 (2013) 1410–1415

[32] P. Tarte, Spectrochim. Acta, 23A (1967) 2127-2143.

[33] A. Tirsoaga, D. Visinescu, B. Jurca, A. Ianculescu, O. Carp, J. Nanopart. Res. 13 (2011) 6397–6408.

[34] F. Bentaleb, E. Marceau, Micropor. Mesopor. Mat. 156 (2012) 40–44.

[35] J.M. Rynkowski, T. Paryjczak, M. Lenik, Appl. Catal. A: General 106 (1993) 73-82.

[36] B. Mile, D. Stirling, M.A. Zammitt, A. Lovell, M. Webb J. Mol. Catal. 62 (1990) 179-198.

[37] M. Lindo, A.J. Vizcaino, J.A. Calles, A. Carrero, Int. J. Hydrogen En. 35 (2010), 5895-5901.

[38] H. Muroyama, R. Nakase, T. Matsui, K. Eguchi, Int. J. Hydr. En., 35 (2010) 1575-1581.

[39] G. Garbarino, A. Lagazzo, P. Riani, G. Busca, Appl. Catal. B: Env., 129 (2013) 460-472

[40] P.Riani, G. Garbarino, M.A. Lucchini, F. Canepa, G. Busca J. Mol. Catal. A: Chem. 383–384 (2014) 10–16

[41] T. K. Phung, G.Busca, Catal.Comm., 68 (2015) 110-115.

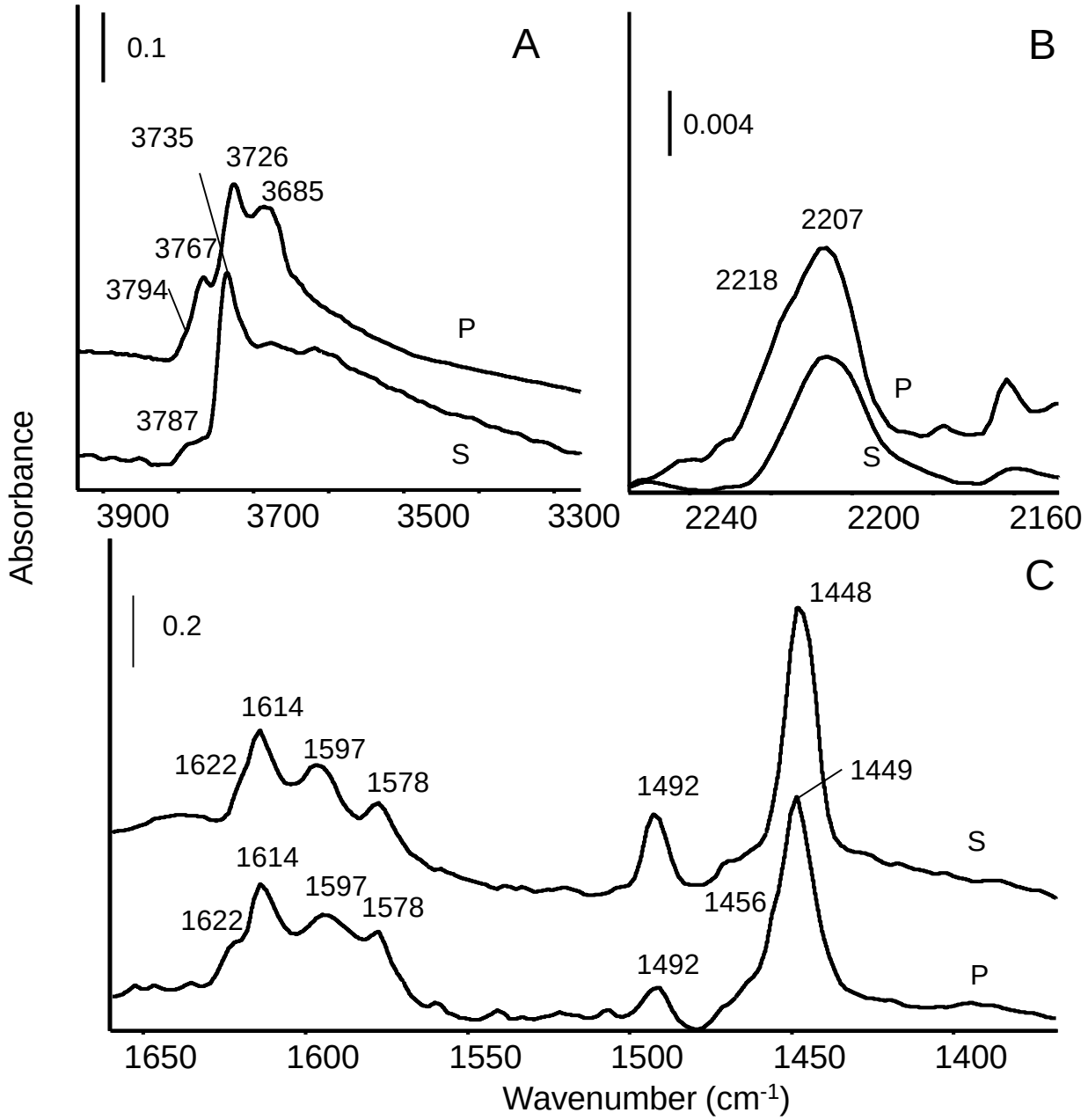
A
0.1
3735
3726
3685
3767
3794
P
3787
S
3900
3700
3500
3300
B
0.004
2207
2218
P
S
2240
2200
2160
C
0.2
1448
1614
1622
1597
1578
1492
1449
S
1614
1597
1622
1578
1456
1492
P
1650
1600
1550
1500
1450
1400
Absorbance
Wavenumber (cm-1)

Figure 1

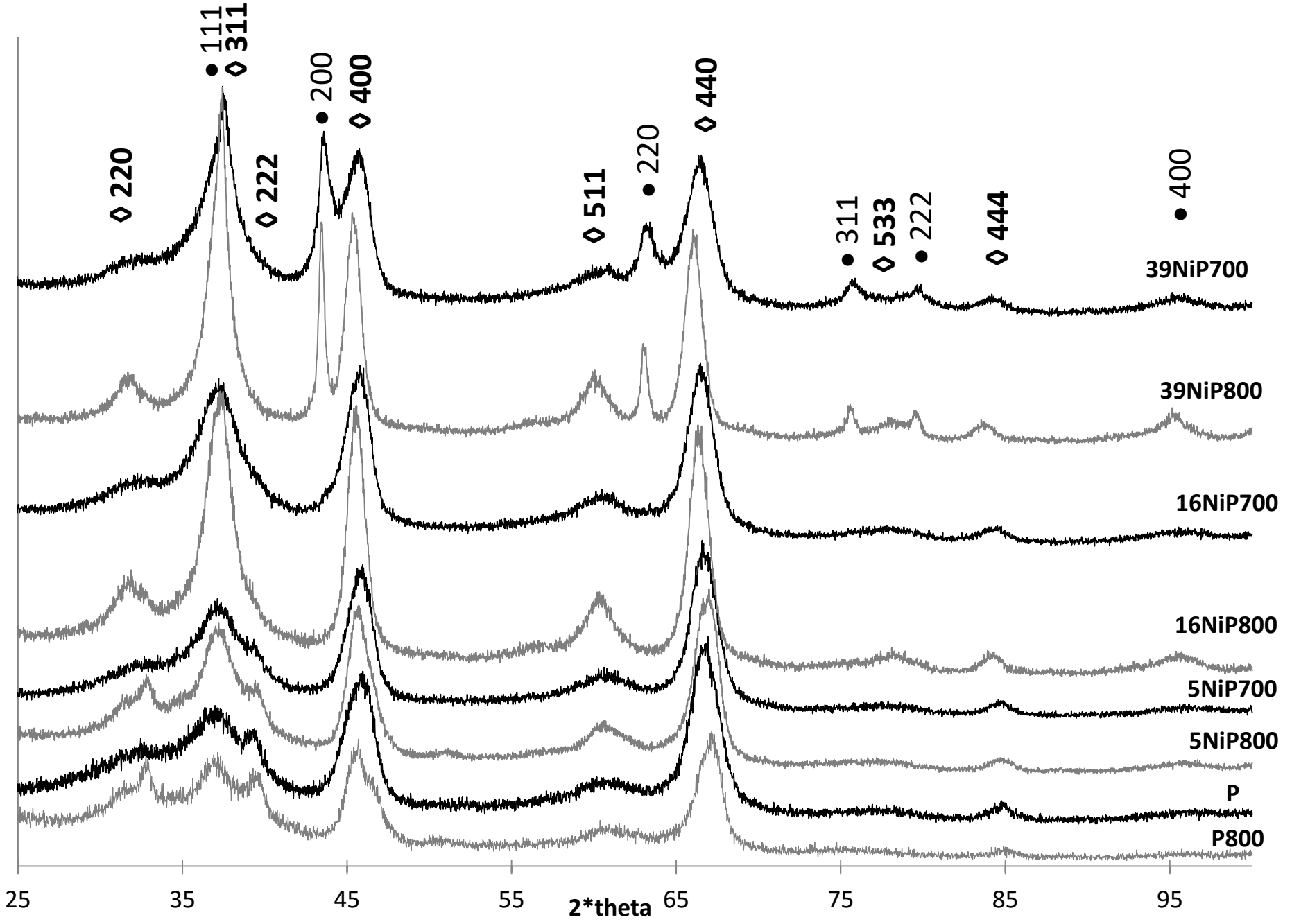
◊ 220
● 111
◊ 311
◊ 222
● 200
◊ 400
◊ 511
● 220
◊ 440
● 311
◊ 533
● 222
◊ 444
● 400
39NiP700
39NiP800
16NiP700
16NiP800
5NiP700
5NiP800
P
P800
25
35
45
55
2*theta
65
75
85
95

Figure 2

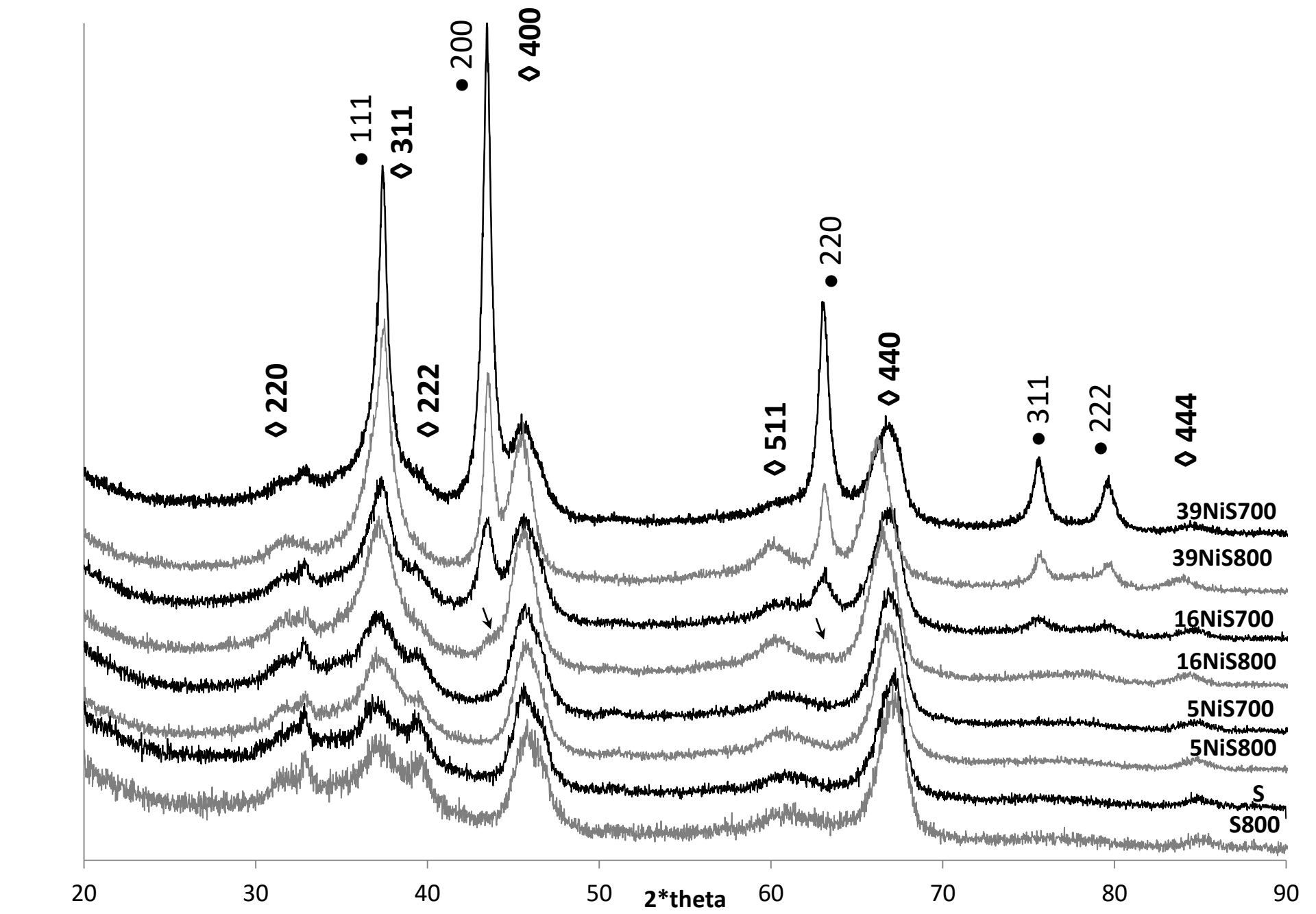
● 111
◊ 311
● 200
◊ 400
◊ 220
◊ 222
◊ 511
● 220
◊ 440
● 311
● 222
◊ 444
39NiS700
39NiS800
16NiS700
16NiS800
5NiS700
5NiS800
S
S800
20
30
40
50
2*theta
60
70
80
90

Figure 3

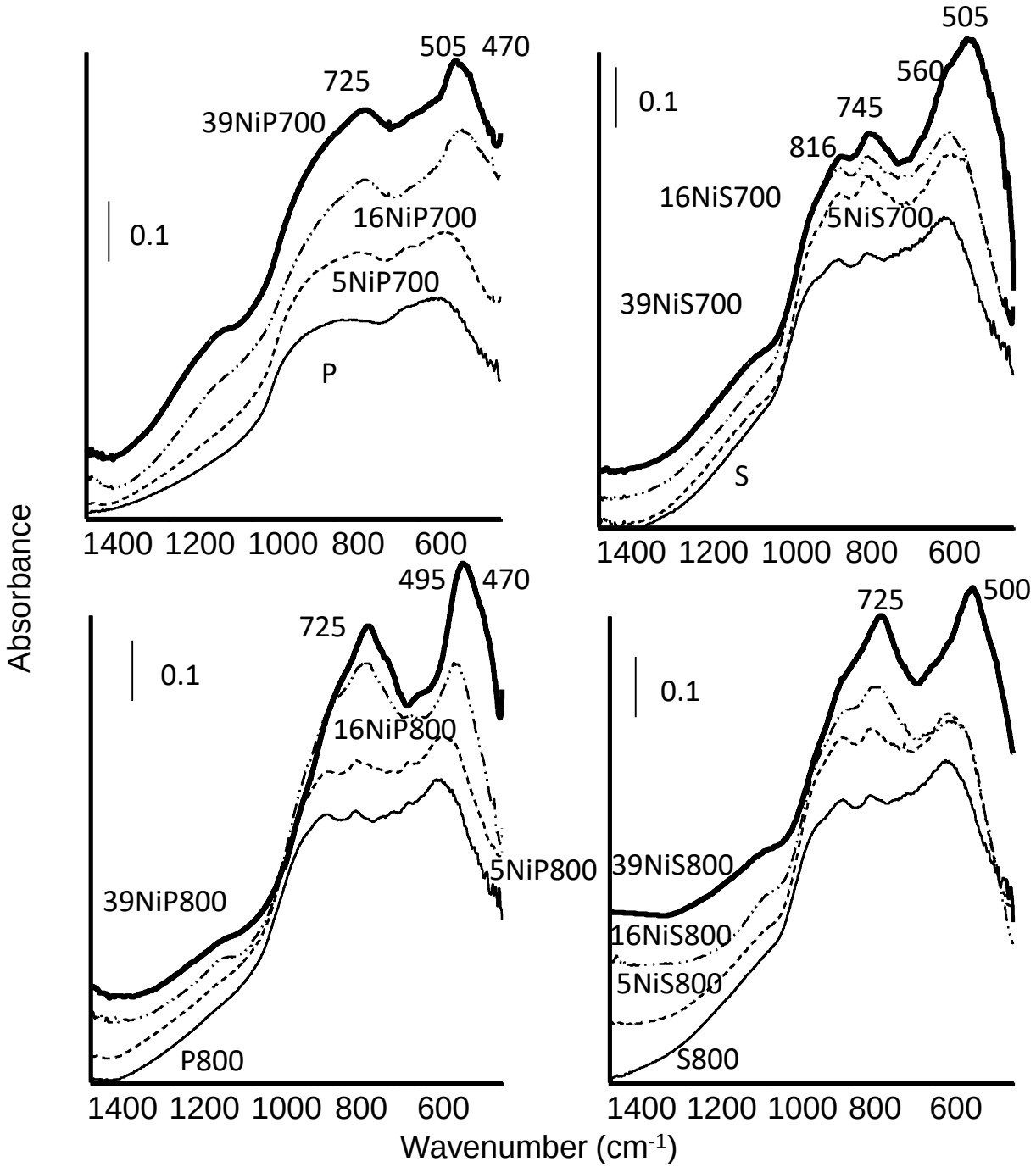
505
470
725
39NiP700
0.1
16NiP700
5NiP700
P
1400 1200 1000 800 600
505
560
745
816
0.1
16NiS700
5NiS700
39NiS700
S
1400 1200 1000 800 600
495
470
725
0.1
16NiP800
5NiP800
39NiP800
P800
1400 1200 1000 800 600
725
500
0.1
39NiS800
16NiS800
5NiS800
S800
1400 1200 1000 800 600
Absorbance
Wavenumber (cm-1)

Figure 4

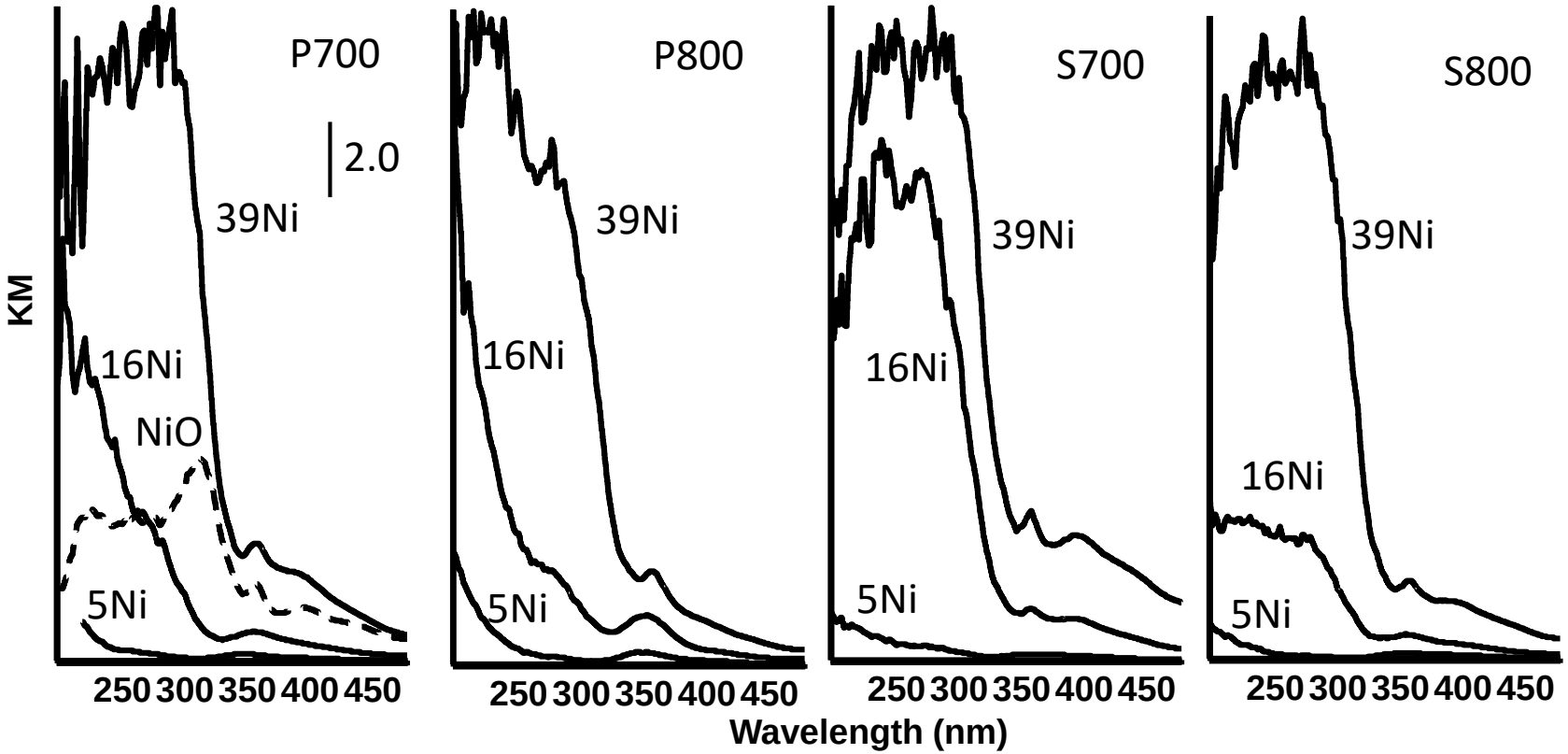
P700
2.0
39Ni
16Ni
NiO
5Ni
P800
39Ni
16Ni
5Ni
S700
39Ni
16Ni
5Ni
S800
39Ni
16Ni
5Ni
KM
250 300 350 400 450
250 300 350 400 450
250 300 350 400 450
250 300 350 400 450
Wavelength (nm)

Figure 5

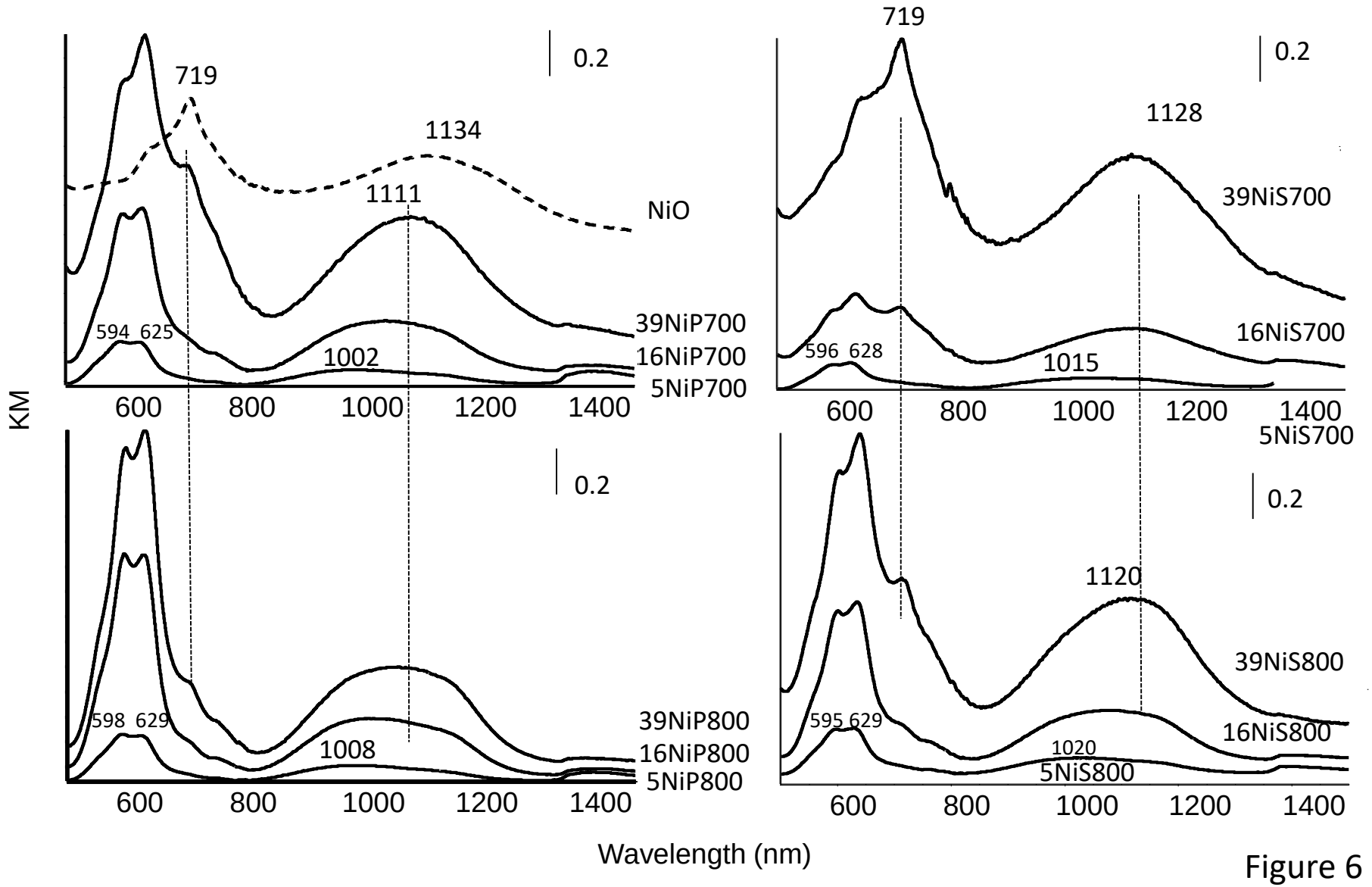
719
0.2
1134
1111
NiO
39NiP700
16NiP700
5NiP700
594 625
1002
600
800
1000
1200
1400
719
0.2
1128
39NiS700
16NiS700
596 628
1015
5NiS700
0.2
1120
39NiS800
16NiS800
595 629
1020
5NiS800
0.2
39NiP800
16NiP800
5NiP800
598 629
1008
KM
Wavelength (nm)

Figure 6

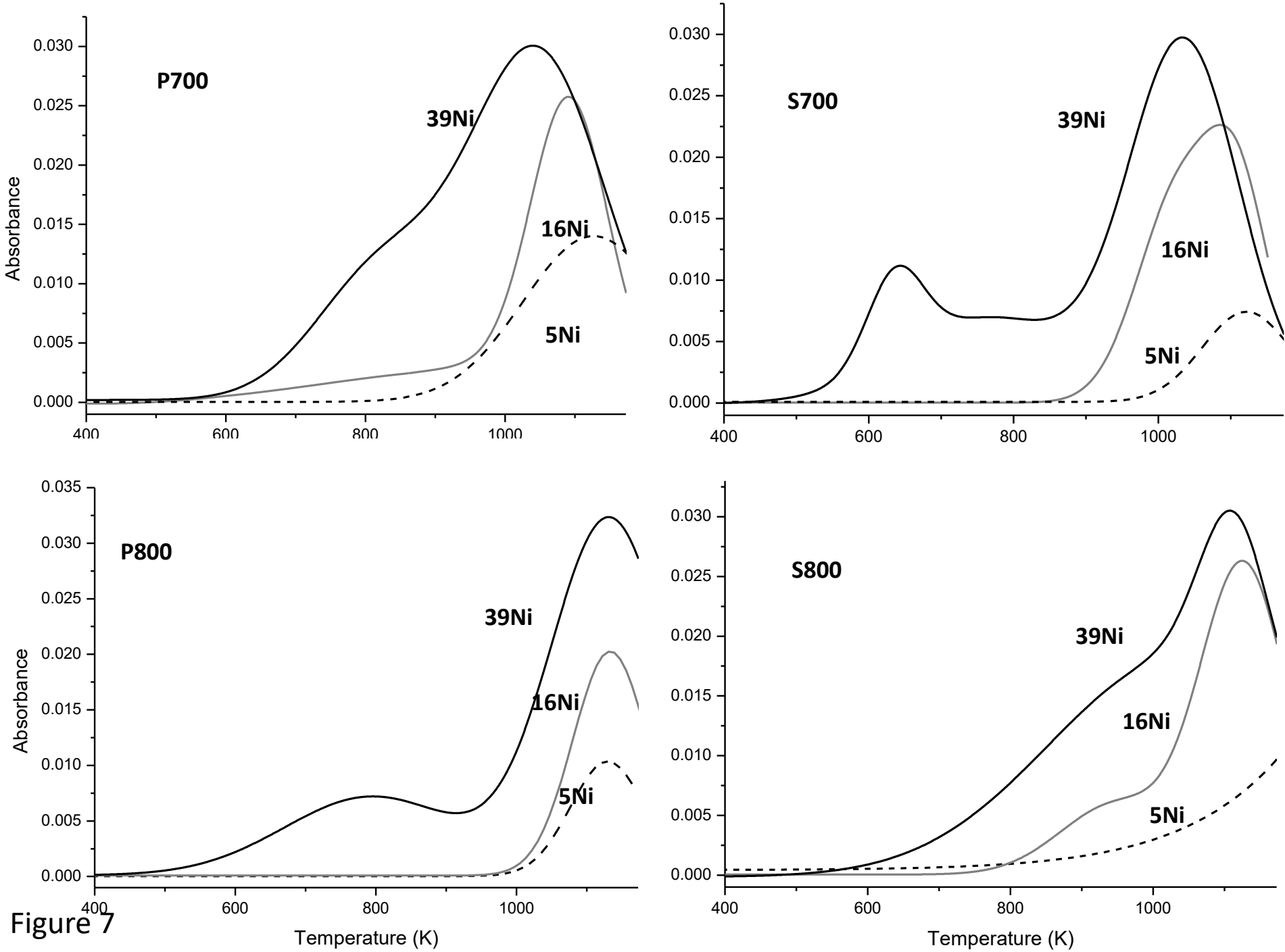
P700
39Ni
16Ni
5Ni
S700
39Ni
16Ni
5Ni
P800
39Ni
16Ni
5Ni
S800
39Ni
16Ni
5Ni
Absorbance
Absorbance
Temperature (K)
Temperature (K)

Figure 7

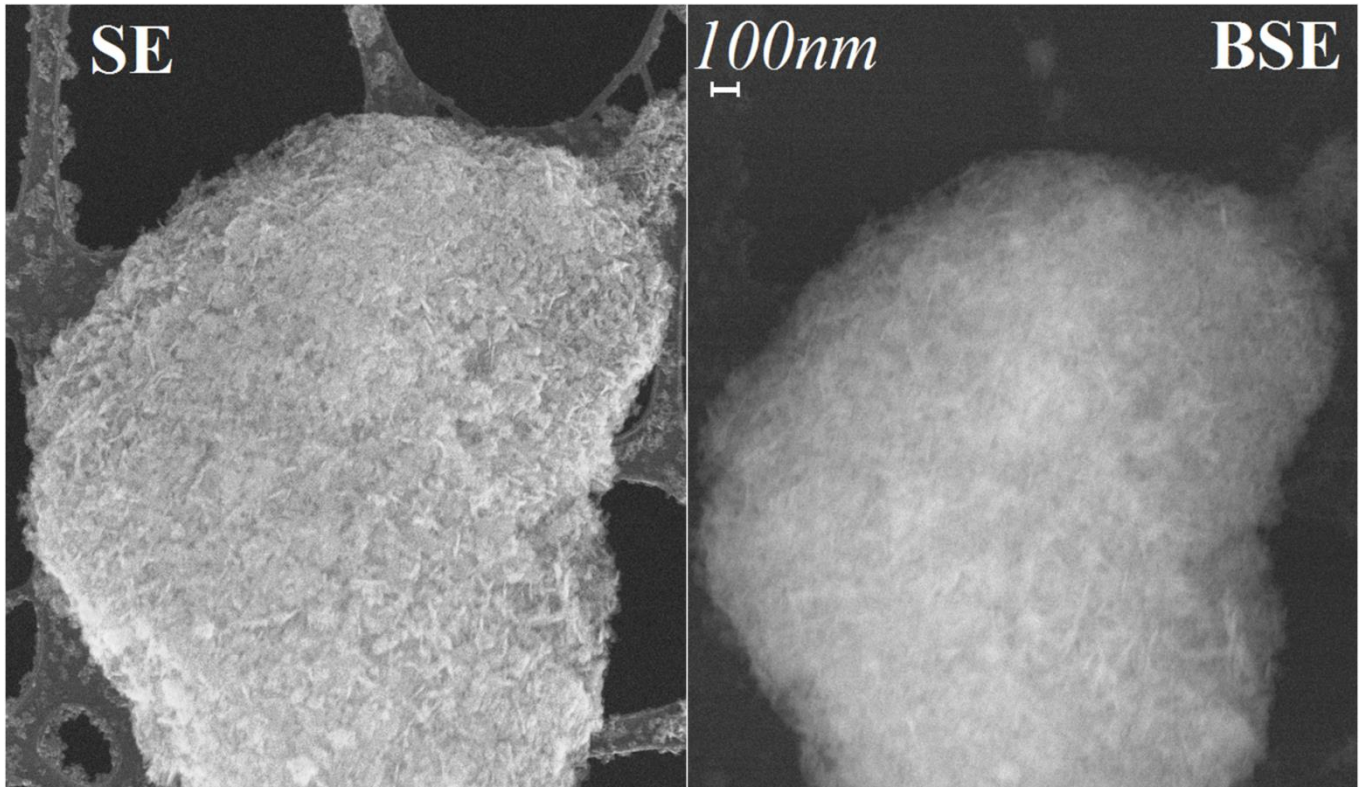

6NiP800

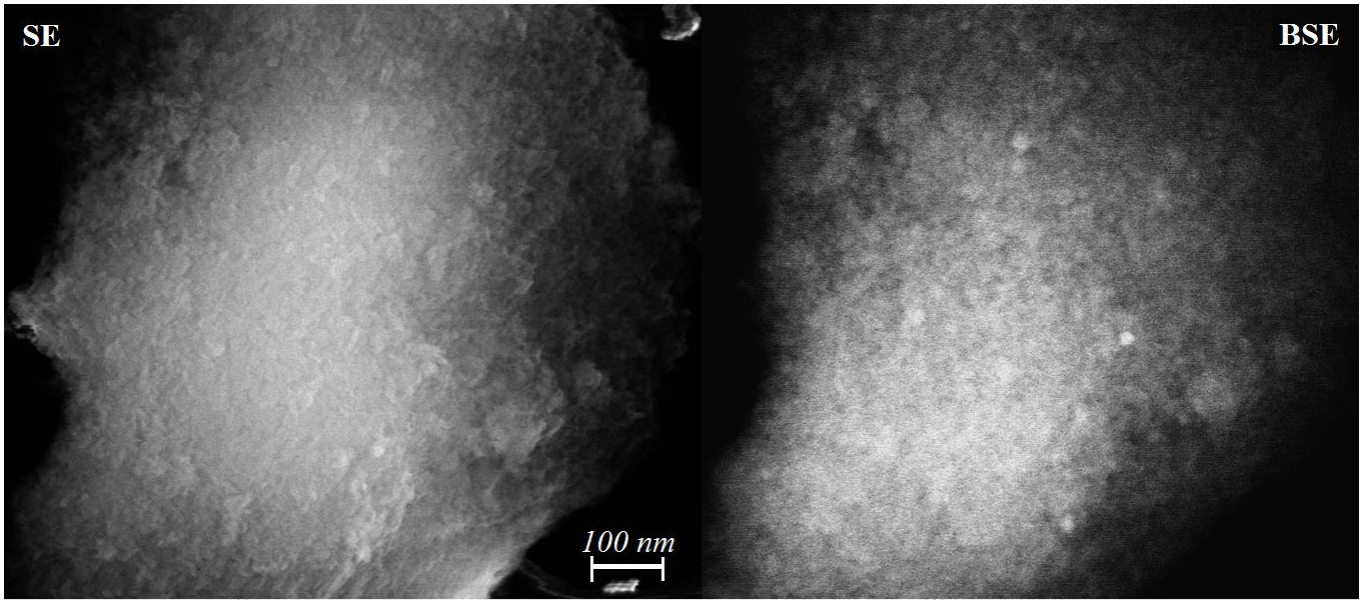

16NiS800

Figure 8

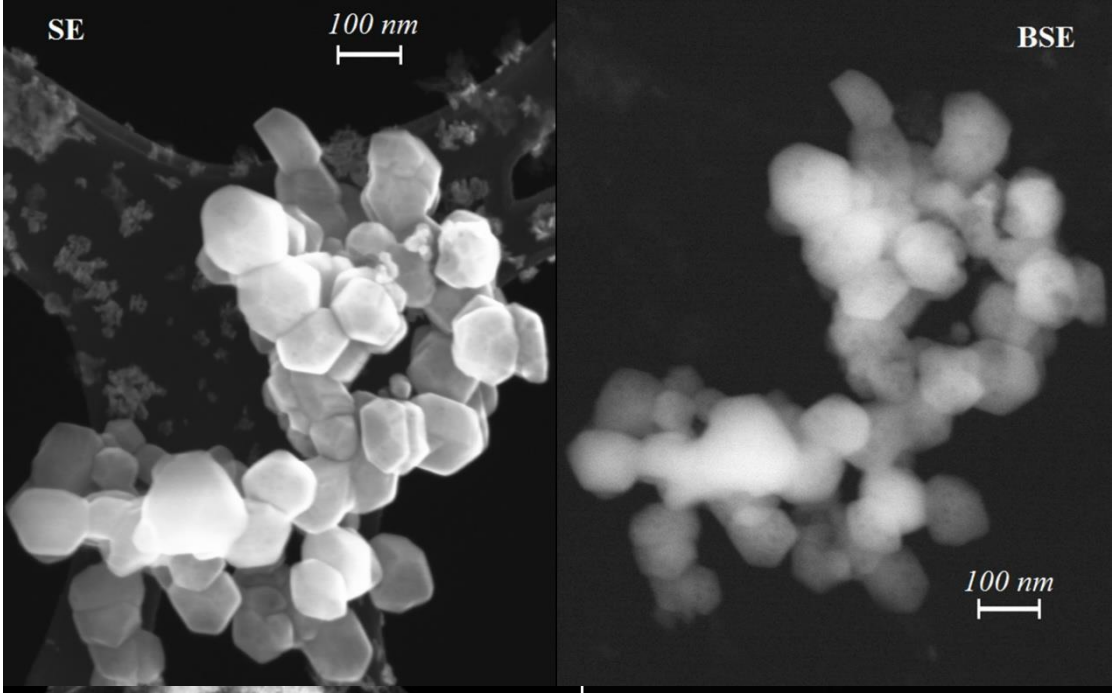

39NiP700

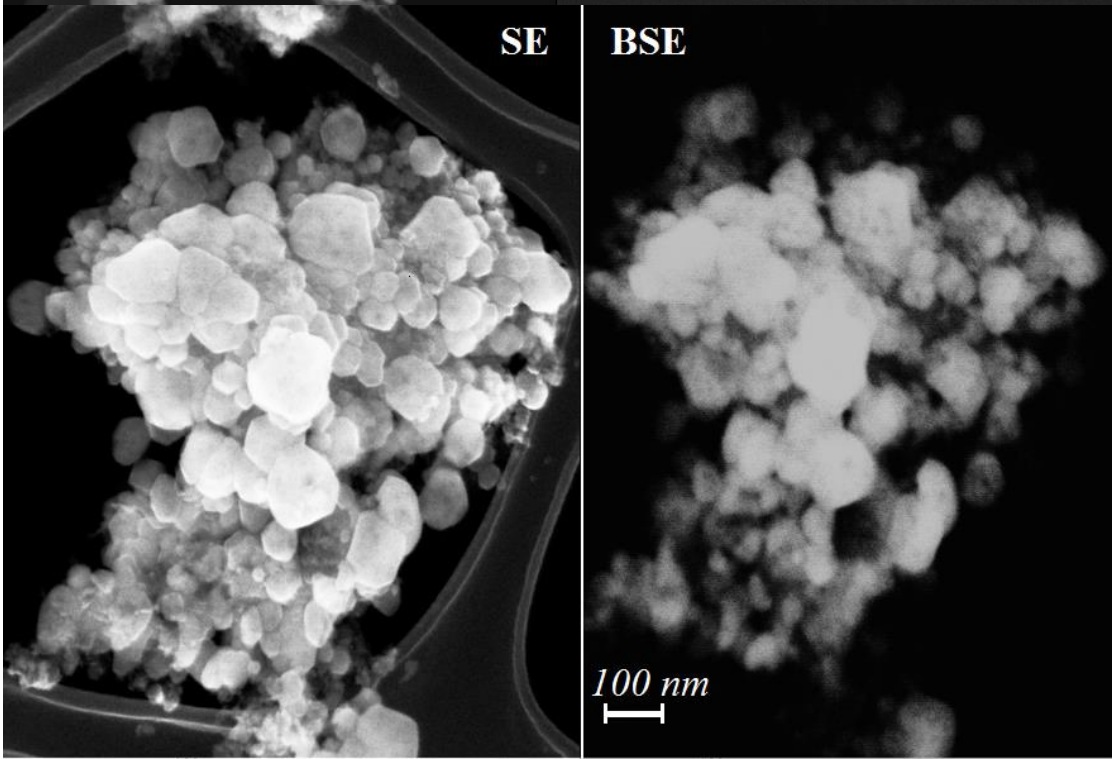

39NiS700

Figure 9